Failure Mechanisms and Damage Evolution of Laminated Composites under Compression After Impact (CAI): Experimental and Numerical Study

X.C. Sun*, S.R. Hallett

Advanced Composites Collaboration for Innovation and Science (ACCIS),
University of Bristol, Queen's Building, University Walk, Bristol BS8 1TR, UK
Ric.sun@bristol.ac.uk (X.C. Sun)
Stephen.hallett@bristol.ac.uk (S R. Hallett)

Abstract

The damage tolerance of Carbon Fibre Reinforced Polymer (CFRP) to Barely Visible Impact Damage (BVID) is a critical design limiter for composite structures. This study investigated the key driving mechanisms and damage evolution of the compressive failure of laminated composites containing BVID using compression after impact and indentation (CAI) tests. Experiments were carried out on two similar quasi-isotropic laminates: $[45_2/90_2/0_2/-45_2]_{2S}$ and $[45/90/0/-45]_{4S}$. Matrix cracking and delaminations were introduced by either low-velocity impact or quasi-static indentation tests prior to the CAI tests. The full-field displacement during CAI as well as the moment of rupture were captured by 3D Digital Image Correlation (DIC). The effect of ply-blocking and influence of factors, such as impact energy, delamination area and surface indentation, on compressive failure was studied. Previously validated high-fidelity finite element (FE) numerical models for the indentation and impact events were then used to investigate the damage evolution during CAI failure.

Keywords: Compression after impact; Numerical modelling; Cohesive interface; Digital image correlation

1 Introduction

Carbon Fibre Reinforced Polymers (CFRP) have become increasingly popular and are gradually replacing traditional metals for applications such as primary structure components in contemporary and future aircrafts. CFRP exhibits superior properties over aluminium alloy like specific stiffness, strength, formability, resistance to fatigue and corrosion performance [1]. Because laminated CFRPs lack reinforcement in the through thickness direction, one of their limiting factors is their resistance to out-of-plane loading such as low-velocity impact and quasi-static indentation. Low-velocity impact, which may occur during manufacture or in service, can result in substantial internal damage without leaving a clear visible trace at the composite surface. This damage is normally called Barely Visible Impact Damage (BVID) [2], which is difficult to detect and easy to be overlooked during general inspection. Hence, there

* Corresponding author: Ric.sun@bristol.ac.uk (Xiaochuan Sun); +44(0) 117 33 15311

is currently a need for a composite structure containing BVID to demonstrate damage tolerant performance under ultimate load.

Matrix cracks, delamination, permanent indentation and fibre failure are damage modes that can occur during low velocity impact, depending on the amount of energy involved [3]. Compared with the residual tensile and flexural performance, the reduction in in-plane compressive strength due to BVID is significant [4,5]. The presence of multiple delaminations reduces the flexural stiffness of the laminate due to the formation of sublaminates, which in turn leads to premature buckling and the reduction of compressive strength by up to 60% [6]. Therefore, the low-velocity impact test [7] in concert with the Compression After Impact (CAI) test [8] is an important design requirement, and the damage mechanisms during loading should be coherently investigated.

Many researchers have investigated low-velocity impact and equivalent quasi-static indentation loading [9–11]. By contrast, systematic studies of damage tolerance in CAI tests are far fewer in number. CAI failure mechanisms during local instability and at the moment of structural failure are thus still not fully understood. Under uniaxial compression, the buckling and failure behaviour of laminated composites with impact damage are strongly influenced by impact damage extent [12–16] and specimen geometric parameters [6,17,18] for a given material system. Amaro *et al*. [19] performed compression tests on cross-ply laminates containing different damage amounts, and showed three different buckling failure modes: pure local buckling, pure global buckling and combined local and global buckling. Relations between material properties, CAI strength, delamination area and impact energy have also been clearly identified elsewhere in the literature. Cartie and Irving [12] found that the CAI response depends on the impact damage threshold load or the toughness of resin system for different material systems. Damage induced below the threshold load has little or no effect on the overall compressive strength. As the delamination area increases and surpasses a critical size as a result of increasing impact energy, the CAI strength drops significantly and then tends to level off, where it is equivalent to a complete perforation of the same size as the delaminated region [12,20,21].

The compressive failure process in thick laminates usually starts with appearance of local buckling (delamination buckling) at the delaminated region and then develops in the direction perpendicular to the loading until the structure collapses [15,22]. In slender laminates with a high width-to-thickness ratio, elastic instability of the entire laminate usually occurs at a low compressive load before or accompanied by the development of local buckling at the delaminated region. In this case, the residual compressive strength/strain might not be acceptable for damage tolerance analysis that takes impact damage into account,

since the structure is in an unstable state before the damage starts to affect the compressive performance [17].

The influence of delamination buckling progression and other factors such as the number and the depth of delamination(s) has been investigated using artificial inserts [23–26]. Pérez *et al*. [27] presented a systematic comparison between CAI properties of laminates with delaminations induced by transverse loading and embedded single artificial delamination. They found that single artificial delaminations irrespective of location, overestimated the residual compressive strength compared to laminates with equivalent actual impact damage. In contrast, Zhou and Rivera [28] found that the compressive behaviour of laminates with artificially embedded delamination was helpful to understand and characterise the response of impact damaged laminate under compression.

As well as the BVID delamination damage, it is possible that the localised contact forces from either impact or indentation can cause surface fibre cracks, permanent indentation and back-face bulging that can lead to fibre fracture crack propagation in the transverse direction. Bull *et al*. [22] performed CAI experiments with micro-focus computed tomography (CT) scanning, offering highly detailed information on the damage progression during CAI. It was observed that a compressive crack near the front surface 0^o fibre plies, caused by previous impact, propagates perpendicular to the loading direction under compression, causing stress redistribution in 0^o plies, which contributes to the residual compressive strength reduction. Rivallant et al [29] also showed the importance fibre fracture in CAI failure mechanisms. In these cases the fibre fracture was important due to either a highly toughened material system being used, causing a reduction in delamination are during impact, or a layup with surface zero plies, which became easily damaged during impact [29]. This reiterates the importance of taking into account both material system and layup/geometry in understanding of CAI behaviour.

Numerical analysis can give a detailed insight into the development of damage modes and the driving stresses, at a level of detail that is usually not possible in experiments, since often they cannot be interrupted and interrogated at critical points. It is however necessary for the models to be based on the correct physical phenomena occurring the tests and to be well validated against a range of challenging data sets. This has been done in the case of static indentation by the current authors in [30] and [31] in which the initial damage and damage progression sequence in quasi-static indentation tests was accurate captured and correlated against detailed x-ray CT scans. Work to this level of detail on modelling of CAI tests to determine the key mechanisms involved is quite limited. Key studies by Hallett and Wisnom [32–34] on other test configurations show that, with the detailed damage modes of matrix cracking delamination and

fibre fracture included in finite element models, good insight of overall failure mechanisms can be achieved. This shows a promising way forward for the future assessment of different material systems and layups for CAI performance. There is however still a lack of experimental detail at the level required to fully validate and test out such models to ensure their robustness is sufficient to act as a fully predictive tool going forward.

This paper presents a series of experimental CAI tests on two different layups, using both static indentation and low velocity impact. A range of delamination sizes were created and tested in compression. One of the major aims of this study was to provide information at the highest level of detailed possible by using data-rich measurements, capturing the entire plate displacement/strain behaviour in three dimensions throughout the whole CAI loading path. Three 3D Digital Image Correlation (DIC) systems allow the capture of full-field displacement at both sides of the specimen during the steady loading stage as well as the moment of failure during CAI tests using high speed DIC. The resulting data is then used for comparison to high fidelity finite element analysis, both as validation of the model and to give further insight into the progressive damage process.

2 Experiment

2.1 Specimen preparation

The material used is the IM7/8552 unidirectional carbon fibre reinforcement pre-impregnated system from the previous studies that created a range of delamination sizes through quasi-static indentation [31] and low velocity impact [35]. In [31], the level of indentation and low-velocity impact energies were set to be above delamination threshold but below back face fibre failure, using either analytical solutions or FE modelling [30,35]. The specimen size and layup was scaled so as to provide configurations with different characteristic delamination responses that could be used as a challenge to numerical modelling and help explain the controlling parameters. All specimens were cut to 150 × 100 mm within 0.1 mm tolerance to ensure the CAI end loading edges were perfectly flat and parallel. This process reduced the chance of unacceptable failure modes during CAI due to stress concentration and load misalignment. Two layups, giving different effective ply thickness, with 4 mm overall thickness, were used. These were denoted as Ply-scaled (Ps) $[45_2/0_2/90_2/\text{-}45_2]_{2S}$ and Sublaminate-scaled (Ss) $[45/0/90/\text{-}45]_{4S}$. Other types of specimens studied in [31] i.e. the 'in-plane scaled' plate ($[45/0/90/\text{-}45]_{2S}$; with in-plane dimensions of 150 x 100 mm) and the 'reference' plate ($[45/0/90/\text{-}45]_{2S}$; with in-plane dimensions of 75 x 50 mm) cases were not used in CAI testing as they are either prone to global buckling due to their span-to-thickness ratio or their in-plane size are not suitable for the ASTM standard CAI fixture.

2.2 CAI test with three 3D-DIC systems

The ASTM test standard CAI fixture [8] (see Figure 1a) was attached to a servo-hydraulic Instron universal testing machine with a 250 kN load cell. The CAI test was performed by displacing the lower grip upwards at a rate of 0.5 mm/min, while the upper grip was kept stationary. To clearly identify the role of buckling (both global and local) during the CAI test, three 3D Digital Image Correlation (DIC) systems were employed to measure the full-field 3D displacements (u, v, w) and strains ($\varepsilon_x, \varepsilon_y, \varepsilon_{xy}$) of both the front (impacted or indented) and back surfaces of the laminate during compression.

A calibration of DIC analysis at the beginning of each CAI test was performed, each specimen was firstly pre-loaded by 200 N with the DIC systems in operation. The pre-load was released, and then the DIC trial results were analysed for calibration. If any significant misalignment, strain concentrations or in-plane strain field asymmetry were detected, the specimen and fixture were readjusted. This process repeated until no such behaviours were observed. Similarly, if any of the above behaviours, as the result of loading imperfections at the interface between specimen and fixture, developed during a complete CAI test, the results were rejected for the best quality possible. The experimental setup for the front and back surfaces of the specimen is illustrated in Figure 1b. Two identical standard DANTEC Q-400 Digital Image Correlation (Std-DIC) systems were placed at the front and back surface of the specimen focusing on the entire visible area. These systems were used to measure the global 3D behaviour of the laminate during CAI test. One high-speed Digital Image Correlation (Hs-DIC) system, that comprises two Photron™ FASTCAM-SA1 high-speed cameras, a stereoscopic setup, high intensity lighting and a computer with analysis software (i.e. Vic3D™), was employed to focus only on the previously damaged region in the centre of the specimen. To capture the local instability as delamination propagated during compressive failure, the Hs-DIC system was activated only for a short period of time just covering the moment of the rupture. Both StdDIC systems had identical resolution of 2448 x 2050 pixel and frame rate of 1 fps, In contrast, the Hs-DIC had a much higher frame rate of up to 30,000 fps but a considerably lower resolution of 512 x 352 pixel. Figure 1a also illustrates the regions of interest (ROI) for the three DIC systems. The three DIC systems measurements gave complete in-plane coverage of the whole specimen and across the whole time-duration of the CAI tests were acquired.

3 Experimental Results and Discussion

The two characteristics of BVID, delamination area and dent depth, of each specimen were measured after 48 hours (due to viscoelastic relaxation). Their correlations with CAI performance of the Ps and Ss laminates are presented in the following sections.

3.1 Compression after Indentation and Impact

Figure 2 shows the residual compressive stress against delamination area with a linear trend line fitted to each data set, and note that the undamaged CAI data points for curve fitting are excluded but presented in the figure. The failure mechanisms of undamaged laminates have a strong dependency on the boundary conditions and are not representative of the actual compressive failure of pristine laminates. Compressive failure strengths for the exact layups used here are not available but results from literature for layups similar to the Ps and Ss cases are 643 MPa [36] for a $[45_2/90_2/-45_2/0_2]_{3S}$ laminate and 675 MPa [37] a $[45/90/-45/0]_{4S}$ laminate. Below the impact threshold energy and static critical force level there is only negligible surface imperfection and a relatively small number of matrix cracks. This damage usually occurs at locations where maximum tension and interlaminar shear are experienced by the laminate during transverse loading [30] and is insignificant to residual compressive performance. The compressive failure behaviour of these specimens is consistent with that of undamaged plates, so those cases were excluded from Figure 2 .

Comparing both layup configurations, the compressive strength reduction roughly scales linearly with the increasing delamination area, similar to the overall trend also reported by Cartie and Irving [12]. Smaller delaminations could be developed during static indentation, below the dynamic critical load. The first data points for the impact tests correspond to the initial delamination area that formed at the delamination threshold energy. Considering both impact and indentation damaged specimens each as a separate group of laminates, a clearer linear relation can be found. These similar tends suggests that the static indentation is not only able to replicate low-velocity impact damage, but also to represent the relationship between impact induced delamination and residual compressive strength.

For the smallest delamination areas induced by static indentation, a sudden drop in residual compressive strength is observed at ~500 mm^2 and ~750 mm^2 in the Ps and Ss cases respectively, as shown in Figure 2. The magnitude of the compressive strength drops are consistent in both cases. The indentation damaged laminate thus seems to become less stable during compression once a critical delamination area has developed. A similar trend was observed by Zhou and Rivera [28], who found a residual compressive damage threshold of 25% of the specimen width, irrespective of shape, orientation and the nature of the damage. Given that the failure mechanisms of all delaminated laminates during compressive failure are similar, this phenomenon in the case of smaller delamination areas is likely to be related to the length of plies in the damaged zone that are free to buckle.

3.2 Dent depth vs. CAI strength

Permanent indentations on the impact/indentation (top or front) surface and a bulge at the bottom (back or bottom) surface, caused by transverse loading, lead to a misalignment between the compressive loading plane and the plate. This misalignment is another factor that should be considered in the study of CAI strength, since permanent indentation (dent for short) is generally considered as a good indicator of BVID in industry. Other studies in the literature [38–41] have considered dent depth (d_{per}) for correlating residual compressive strength with damage developed during transverse loading.

In this study, the front face dent as the distance to a best-fit-plane of the specimen surface were measured with the 3D-DIC system. Figure 3a plots the CAI strength against dent depth with a linear trend line for both loading conditions and laminate configurations. In general, the CAI strength decreases with increasing dent depth. The linear fit for the Ss laminates was found to have a better correlation than the Ps case, but the gradients of the fit line for each laminate configuration are fairly similar. The initial dent depth corresponding to minimum delamination damage size consistently starts at about 0.1 mm in both impact and static loadings and for both types of laminates, as shown in Figure 2b. Those curves do not collapse onto a single master curve in both plots in Figure 2, showing that whilst it is often used in industry, dent depth is not a particularly good general indicator of CAI strength. A large variation in delamination area can be seen for any given dent depth, which implies that the permanent dent is dependent on transverse loading rate and ply thickness as well as delamination area.

4 Global CAI behaviour: results of standard DIC systems

To determine the plate response during CAI, and to investigate how the surface deformation is related to the compressive damage mechanisms, 3D relative displacement changes of the front and back surfaces of the laminates were obtained from the DIC systems and analysed. With the exception of the undamaged laminates and laminates containing only minor matrix crack damage, all delamination damaged specimens failed by the same damage mode according to the ASTM CAI standard [8]. This damage is caused by delamination propagation along the width direction, accompanied by fibre failure, starting from the central underlying delamination area, as shown in Figure 4. Some results were rejected due to a significant misalignment or strain localisations developed during CAI tests. The rest of the results were analysed, post-processed and then studied. Because of the consistent failure behaviour in all damaged laminates, only DIC results of a post-impact Ps and post-indentation Ss laminates are presented and discussed here.

4.1 Global displacement profile

The DIC systems used in the CAI test can easily identify global buckling. The deflection profiles from a DIC system can also be compared with results obtained from mechanical testing machines to verify their reliability. Looking at the out-of-plane displacement profiles generated from the two Std-DIC systems at both sides of the specimen and at the 'branch out' from initial stiffness in the load-displacement curves generated from the test machine, no strong evidence pointing to the occurrence of significant global buckling during CAI, prior to final failure for the Ps and Ss laminates was found.

Figure 5 and Figure 6 show the Std-DIC results of the CAI test of a post-impact Ps and post-indentation Ss laminates. The reason that these two cases have been compared is that they have similar size of delaminations (i.e. 1350 mm^2 and 1474 mm^2 for the Ps and Ss laminate, respectively), similar dent depth (i.e. 0.1455 mm and 0.1686 mm for the Ps and Ss laminate, respectively) and similar level of final failure load. And the profiles of the projected delamination prior to CAI test for both cases are illustrated in the Figures. Each figure provides four snapshots of the global out-of-plane displacement (w) contour of both the front and back surfaces of the specimen at increasing compressive loads. The first frame of both cases was selected after the deflection of the surface dent becomes obvious, while the final frame was taken immediately after the CAI rupture. Each Std-DIC system operates independently and does not communicate with the other. The results generated by each system are mapped to its own individual coordinate system based on the reference frames that were taken at the beginning of each CAI test. This means the initial surface imperfections caused by impact and indentation force form part of the baseline profile and deflections are measured from this. For each system, a positive 'w' means that for a given point it has moved from its original position in the reference frame closer to the DIC system, and away from the DIC system for negative values.

It can be seen that the local deflection originated from the delaminated regions and becomes significant at about half of the failure load for both cases. These deformations can also be considered as local nonlinearity and buckling of the delaminated region, which progresses as loading is increased. The evolution of the deformation zone includes increase in its amplitude and width. This phenomenon is influenced by the misalignment created between the line of action of the loading and the plane of the laminate at the damaged regions, which leads to the formation of bending forces acting at the boundary of the dent and bulge regions. The evolution of local out-of-plane deformation seems to be a stable process as the load increases until sudden rupture occurs. During the stable stages of deformation evolution, both front and rear deflections are in the direction of impact/indentation loading. At the point of unstable rupture the

back face bulge region continues to deflect in the same direction, while the front face dent region, in contrast, snaps through to the deflect in the opposite direction to impact/indentation loading. This leads to a bulging of both surfaces in each case, as shown in the last contour plot in Figure 5 and Figure 6. This behaviour was found in most of the delaminated laminates during compressive failure and was independent of ply thickness and the method of previous transverse loading types i.e. impact or indentation. It is worth noting that, in comparison with the pre-existing delamination profiles, the band of deflection is narrower, in the Ss case than in Ps case in the direction of CAI load and width direction; this is probably because the delamination propagates more easily in the thick Ps ply blocks.

In contrast, studies in the literature [4,22,29] showed that laminates that have experienced higher energy impacts resulting in fibre fracture tend to exhibit local buckling towards the impact direction during CAI. The same studies also observed fibre fracture near the front surface due to compression during impact, leading to stress redistribution and stress concentration under subsequent CAI. However, the connection between fibre compressive fracture propagation and local buckling as a result of delamination growth is still not straight forward.

4.2 Local buckling stiffness at delaminated region

In order to identify at which point the deformation becomes significant enough to affect local buckling and delamination propagation, Figure 7 shows the transverse deflections of a point at the centre of impact (initial dent) and the corresponding point at the back face bulge centre, plotted against compressive stress during CAI tests of the Ps and Ss laminates earlier presented in Figure 5 and Figure 6. This is recorded up to but not including the final catastrophic event where the front side sublaminate suddenly snaps through to large positive displacements, as indicated in the cross-section plots of Figure 8b. The transverse deflections of each case are subjected to the pre-defined global coordinate system, which allows thickness change to be indicated as the gap between the two curves for given stress levels. The local buckling load is usually defined as the load level that corresponds to the moment that the relation between transverse deflection and compression becomes nonlinear.

All curves consistently follow a clear transition from linear to nonlinear, marked by a ‘knee point’, A, at the intersection of two linear trend lines, shown in red in Figure 7. The load level at this knee point can be characterised as the local buckling load. A separation of the two initially aligned deflection curves also occurs around this point. The corresponding local buckling loads correlate well with the load level of the first obvious local deflection in the global deflection contours (see Figure 5 and Figure 6). The transition of buckling stiffness is smooth and steady (see Figure 7). The region away from the lower interfaces of the

laminate after local buckling onset is still not fully damaged, and the laminate can thus bear flexural loading until delaminations grow further, which explains the roughly linear buckling stiffness after the knee point. As the number and the size of the delaminations increase, the laminate effective flexural stiffness decreases. This, together with the development of local buckling, perhaps explains the nonlinearity of the deflection curves near failure. Finally, due to the large deflection of the delaminated sublaminates and the delamination growth, the delaminations become unstable and lead to plate collapse. The deductions made from the DIC results on the damage evolution can be verified and further analysed by the high-fidelity numerical models presented in section 6.

4.3 Whole specimen displacement measurements: standard DIC results

A number of studies have reported experimental observations of CAI tests and summarised the possible out-of-plane behaviour by presenting cross-sectional schematics of the composite plates [20,42,43].These plots are based on deflection measurements taken at specific points on both surfaces of the laminate during CAI tests. Inevitably, when drawing a cross-sectional variation under compression, deflection at locations where no measurement is provided need to be speculated according to theoretical buckling behaviours. These schematics effectively represent the top and bottom sublaminate local buckling mode, helping one to intuitively understand the buckling behaviours. Here full-field measurements from the DIC systems from both sides of the laminate during CAI test allows thousands of points to be captured simultaneously, covering most of the laminate surfaces, providing reliable experimental observations. Out-of-plane displacement of a control line that is parallel to the loading direction and across the initial damaged centre was obtained from each of the front and back surface DIC results. Since each DIC result was based on its own reference image, in different individual coordinate systems, the two line results were then mapped into the global coordinate system that was previously defined with taking into account the actual laminate thickness, shown in Figure 8. The figure shows the out-of-plane displacement behaviour observed in one of the Ps experiments. The values at 2 mm are at the front face and show local buckling into the laminate, in the same direction as the previous transverse loading. The values at -2 mm are at the back face and show local buckling in the opposite direction (bulging outward).

As previously observed, significant global buckling is not present during CAI tests. Similar to the global defection contours shown in Figure 5 and Figure 6, the development of the dent and bulge become obvious at compression loads higher than local buckling load, and their amplitudes increases with increasing compression. After a steady growth at the damaged regions, the back surface bulge and front surface dent suddenly go unstable, leading to overall compressive failure of the plates. The missing data

points on the front surface curve in Figure 8b at the failure step is due to the paint-based speckle pattern coming off at the moment of final sudden rupture.

5 Local displacement at rupture: high-speed DIC results

The front surface buckling in the opposite direction of transverse loading as one of the final failure behaviours is commonly observed in CAI tests. However, few studies are focused on the surface response of the plates at the moment of final rupture, with plausible explanations. Mostly, the studies are limited by the experimental data available, especially since the duration of the rupture moment is of the same order of magnitude as a crack propagating across the width of the laminate. It is believed that the failure mechanisms of CAI at rupture are as important as the CAI failure mechanisms prior to failure, and this is critical for understanding the origin of instability and final failure, as well as being informative for numerical model validation.

In this study, the transient surface deflection was captured by a 3D-DIC system using high-speed cameras (Hs-DIC) which focused on the region of interest just covering the initial dent and bulge regions at front or back surfaces, but not simultaneously in the same test. The frame rate used to capture the response at the moment of rupture was up to 30,000 fps. The time duration of the failure rapture was around 0.2 ms. Figure 9 shows out-of-plane displacement contour plots measured from four consecutive frames taken by the Hs-DIC system for the back face of a post-impact Ss laminate. Similar to results given by the Std-DIC system, the deflection from Hs-DIC is based on the correlation with the reference frames taken at the beginning of the CAI tests. It can be seen that the local buckling of the back surface develops in amplitude and expands rapidly in the direction perpendicular to the compression load until the local instability reaches the edges of the laminate. It is unknown to what extent this surface response represents the behaviour of sublaminates inside the specimen, but this suggests that the instability firstly occurs at the centre of the laminate at the most delaminated region and then propagates in the lateral direction. It is uncertain at which surface the local buckling happens first to trigger the final rupture, since simultaneous measurements on the same specimen could not be recorded due to only one pair of high-speed cameras being available.

Compared to the propagation of deflection and delamination at the back face, the response of the front surface at the damaged region during CAI failure for most of laminates tested was more complex, and the detailed front surface deflection field of laminates tested was not consistent. Figure 10 shows the out-of-plane deflection profiles of the Ps and Ss laminates with impact and indentation damage. Each plot is the first frame taken by Hs-DIC after the Hs-DIC system is triggered. It is observed that the front face

outward displacement is formed before the final rupture and its peak is above (Figure 10b &d), below (Figure 10a) or surrounding (Figure 10c) the initial dent region. This front surface deflection can also be seen in Figure 11 which illustrates the development of out-of-plane displacement at the front surface at the moment of rupture in a post-impact Ps laminate. The time interval of each frame is ~ 0.06 ms.

Although the formation of the front surface deflection cannot be captured by the Std-DIC system, a location shift between the dent trough and peak of the front surface deflection at CAI failure can be seen in the cross-section profile (see Figure 8), which matches the Hs-DIC results. The development of initial dent and the formation of the front surface peak are also indicative of full through-thickness buckling. Since the magnitude of the peak of surface deflection is higher than the dent trough, the delaminations under the peak can open up. In contrast, through-thickness compression developed by the dent trough tends to close the underlying delaminations, causing more localised and reduced magnitude of deflection compared to the peak. During the CAI failure, the front surface peak region starts growing and expanding in the lateral direction (see Figure 11).

6 Numerical modelling of compression after impact

6.1 Model description

The concept of the CAI finite element models was in line with the modelling techniques used in previous studies for the indentation and impact modelling [30,35]. All analyses were conducted using the explicit finite element solver LS-Dyna. Models were created at the mesoscale, with each ply being modelled with a single layer of continuum hexahedral elements. Between each ply with different fibre orientation, there was a layer of cohesive interface elements, and within each ply six potential matrix cracks were included (using cohesive interface elements), passing through the indentation/impact zone. After the completion of static indentation or low-velocity impact virtual testing, the failed cohesive elements at inter- and intra-laminar regions were grouped together and given minimal cohesive properties in the subsequent CAI simulations. This represents the delamination and matrix cracking, but allows the CAI laminate model to retain the internal nodal connectivity at the damaged regions and eliminate numerical instability. The compressive behaviour of the cohesive law also modelled the contact between the cracked surfaces. The material properties of the rest of the intact cohesive elements and solid elements in the plies were identical to those in the previous impact/indentation laminate models and are given in Table 1.

As shown in Figure 12, the CAI fixtures were modelled according to the actual dimensions of the experiment (see Figure 1). The lateral expansion constraint given by the two side blocks was simulated by

restraining the two planes of nodes along the long edges (Plane *ZX*) from translating in the *Y*-direction. The top and bottom clamps and two pairs of anti-buckling guides were modelled as rigid material, with a surface based contact to the laminate. One of the clamps was held stationary in the simulations, and the other given a prescribed motion of 0.5 mm/s. The *X* directional contact force generated between the moving clamp and the laminate was used to measure the compressive load. Once the delamination propagation reached the anti-buckling guides, the simulation was considered to be complete and then terminated. Mass scaling was used to achieve reasonable run times, with the model output being carefully monitored for dynamic effects.

The experimental observations show that there is no clear difference in residual compressive strength between post-impact and post-indentation laminates (see Figure 2). Thus, the residual compressive behaviour of damaged laminates was studied numerically here did not consider the type of the transverse loading applied, but instead was based on a given delamination area (taken from indentation models). The CAI simulations for the Ps and the Ss cases with four different damage sizes for each layup were performed. Since it was found in DIC results that the surface imperfections (dent and bulge) have an influence in local surface deflection during CAI tests, the permanent dent and bulge were manually introduced for all CAI models, since the indentation/impact models for the delamination damage did not have capacity to predict this. The dent depth introduced for both laminates was according to the experimental results trend line shown in Figure 3a.

6.2 Numerical Results and Discussion

6.2.1 Load-displacement relation

The models had pre-existing delamination diameters of 20 mm, 30 mm , 40 mm and 50 mm are referred to D20, D30, D40 and D50 and as a suffix to each laminate, for example Ps plate with pre-existing delamination area of 20 mm diameter prior to CAI virtual testing is referred to Ps_D20. Figure 13 plots the correlation between delamination area and CAI strength for all tests. It shows that the modelling results conform to the general trend of the experimental results for both loading cases and both laminate configurations when delamination is smaller than 1200 mm^2. The CAI models in all cases capture the sublaminate-scaling effect on the CAI strength with predicted CAI strength of the Ss case being higher than that of the Ps case for roughly the same delamination area. The differences between CAI strengths becomes smaller as the delamination area increases. As delamination increases, the predicted CAI strength reduction of the simulations starts to level off for both Ps and Ss laminates, as shown in Figure 13. Possible reasons for the reduction of correlation with the larger damage size are: the intra-laminar splits only exist in the model in the central region and for the largest delaminations may not be sufficient in number, the mesh size

is increasing away from the impact/indentation event, and surface damage may be increasing in the experiments with increasing energy, but was introduced in the models over a constant area.

Similar to the local buckling curves obtained from Std-DIC systems, buckling curves derived from the CAI modelling of a small (D20) and large (D40) delamination are shown in Figure 14a and b, respectively. The D40 case in Figure 14b can be compared to the experimental curves in Figure 7 since the delamination areas are similar: the ~40 mm diameter delamination gives 1257 mm^2 vs 1350 mm^2 and 1474 mm^2 for the Ps and Ss experimental laminates from Figure 7. As the boundary conditions in the FE modelling provide ideal in-plane constraints and the plate is perfectly flat, without any imperfections other than the delamination damage, there is a stiffer initial response and a clearer transition from global behaviour to local buckling than in the experiments. The transition occurs at slightly higher loads than the experiments, again due to the ideal constrains and lack of imperfections. The curves from the front and back faces of the CAI models are highly aligned up until the compressive stress level reaches ~ -280 MPa (-112 kN) for the D20 case and ~-200 MPa (-80 kN) for the D40 case, after which a snap-through behaviour was observed, as in the experiments. Divergence of the front and rear face deflections was however more gradual in the experimental case.

6.2.2 Detailed Damage Predictions

The CAI virtual test was able to capture the final stages of delamination propagation for interrogation in a way that is not possible in the experiments. Similar local behaviour and damage growth sequences were found across all CAI models. The post-indentation Ps_D20 laminate was selected and is presented here for detailed analysis and investigation. Figure 15 shows the development of delamination damage at the four increasing load levels (F_i). F_1 (121 kN) is the load level at which the delamination start to propagate and F_{cf} (134 kN) is the compressive failure load at which the delamination propagation reaches the vertical edges of the laminate. The load steps F_2 and F_3 immediately after F_1 and before F_{cf} are 134 kN at 126 kN and 132 kN, respectively. Figure 15 shows that the delaminations grow perpendicular to the loading direction and that propagation in the loading direction is relatively minor. The modelling results are also in line with other experimental observations found in available studies in the literature [6,15,43]. It also shows that the growth of pre-existing delaminations under static compression can be divided into an initially stable and then unstable process. When delaminations start to rapidly expand in the lateral direction, the process becomes unstable.

To gain further understanding of the final failure process, Figure 16 illustrates the progressive buckling behaviour and cross-section changes at the four previously defined compressive loads. Cut-section

views are plotted for each stage. The CAI models capture the increase in the post-impact/indentation surface imperfections (front-face permanent dent and back face bulge). At F_1, the back-face bulge starts to develop, and this corresponds to growth of the rear delaminations (Figure 16a and b) and full through-thickness buckling of the delaminated section of the laminate. Since the delaminations are larger below the mid-plane than at the upper interfaces, the lower plies to have longer unsupported regions and to tend to buckle outwards. As the top dent grows, an adjacent front surface bulge starts to form, pushed up by the buckling plies and sublaminate below it (Figure 16b). This is in accordance with the experimental observations captured by Hs-DIC system (see Figure 10 and Figure 11). Finally, the CAI laminate model fails by simultaneous propagation of the delamination and the full through-thickness buckled region to the plate edges with most of the plies at the delaminated region being buckled towards the lower surface. Figure 17 also shows the changes in cross-section during CAI for a sublaminate scaled case (Ss_D20) up to compressive failure. One of the noticeable differences between the two layups is that the width of the deflection band (i.e. the width of buckled plies) at both surfaces in the Ss case is much smaller than in the Ps case, which is in line with the Std-DIC results shown in Figure 5 and Figure 6 and also in a good agreement with the experimental observation shown in Figure 4a. At the failure stage of the Ss case (Figure 17d) roughly an equal number of plies buckle outward in each direction. The general cross-section behaviours of both the Ps and Ss cases containing similar delamination areas are alike and agree with the Std-DIC results (see Figure 8b), which give confidence in the accuracy of the prediction of internal damage behaviour in the FE models.

The simulations capture the buckling behaviour of the plies with delamination growth, but the experimental final failure was also accompanied by fibre failure as well (see Figure 4). Fibre failure is not included in the current CAI simulation approach as a progressive failure model. However, in order to confirm if a basic fibre direction maximum stress criterion was exceeded, the model output was post-processed at each loading increment during the final stages of the test to assess the maximum compressive stress of loading bearing plies (0^o plies). Figure 18 shows the 0^o ply longitudinal stress in the Ps_D20 and Ss_D20 models once major delamination propagation has started; the ply with the maximum compressive stress is presented for each case. These stresses are below the compressive strength of 1690 MPa for the IM7/8552 material [44] and the delamination propagation occurs prior to compressive failure of the ply for both cases. As local buckling increases, fibre compressive failure will occur near final CAI failure. However, it can be stated with confidence that in these cases the CAI failure is initiated by local buckling and the

associated delamination propagation. However, this may not be the case if fibre breakage exists prior to the CAI test or for different layups and materials.

The full-field measurements from the DIC systems not only provided data-rich experimental results but also allowed the high-fidelity modelling to be validated in the highest detail possible. Surface deflection profiles that were measured by the DIC systems on the both side of the laminate during the CAI tests can be used to validate the numerical simulations. Figure 19 shows the front face out-of-plane deflection profile at the four compressive loading stages defined previously. If compared to the experimental results shown in Figure 5, the front surface dent in-plane dimensions are underestimated (see Figure 19). Although, the CAI laminates with an artificial dent and bulge have the similar geometry of the post-impact/indentation laminates at the start of the analysis, any local degradation of the plies (other than the included matrix cracks) is not taken into account as plies are modelled with elastic material properties. Nevertheless, the CAI model captures the local buckling behaviours of both surfaces, especially the formation of the front surface deformed shape (upper-right plot in Figure 19), which is very similar to the Hs-DIC images as shown in Figure 11.

6.2.3 Damage Evolution Predictions

The high-fidelity CAI FE models give good predictions of the failure load and local buckling behaviour for the range of layups, loading cases and delamination sizes tested. Therefore it is assumed that the correct physical phenomena are captured in the numerical model for the damage evolution and damage mechanisms leading up to the CAI failure. These can thus be further interrogated in the model results for deeper understanding of the failure driving mechanisms. Figure 20 shows the prediction of a damage sequence during the CAI failure. It is noted that, for the sake of illustration, the laminate models plotted here are all based on the geometry of the initial undeformed state of the CAI laminate model, and the matrix cracks (intra-laminar elements) are omitted from the plot. The pre-existing and newly-created delaminations during compression (failed cohesive elements) are shown. The first delamination growth occurs at the interfaces near the bottom ply due to outward (bulging) local buckling of the lower most plies (Figure 20c). This initial damage growth can be correlated with the Std-DIC results in Figure 8b, which shows an apparent increase in thickness implying the delamination growth near the back surface. A delamination-free zone that is beneath the impactor or indenter was observed in all specimens tested and predicted by the high-fidelity models (Figure 20b). Delamination propagation into this undamaged cone is considered as the second important event in damage mechanisms. Similar behaviour was also observed by Bull et al. [22] using micro X-ray CT-scan. Figure 20d shows delaminations growing at the lower interfaces

and also start to propagate into the undamaged cone from its periphery. The complete growth of delaminations into the undamaged cone is shown in Figure 20e and is followed by strong local buckling as a result of delamination growth at each available interface. Once the delaminations have fully formed in the central region, there is sufficient loss of local stiffness such that the whole cross section can buckle through the thickness (see Figure 16c &d) and then unstable delamination starts to propagate across the width of the laminate (see Figure 15d).

The interaction between matrix cracks and delaminations did not seem to be significant during the CAI failure, as the matrix cracks propagation was not obvious until the front surface started to buckle to the opposite direction (outward). To confirm that the matrix cracking did not play a significant role in the CAI failure mechanisms, CAI simulations of selected models Ply-block laminates (Ps) with matrix cracking disabled were performed. In these models, the pre-existing failed and intact matrix crack cohesive elements from the impact or indentation simulations were assigned to laminate properties in the CAI simulation, so that those elements no longer behaved as cohesive elements but normal 8-node solid elements. By comparing CAI models with and without matrix cracking, it was found that the predicted CAI strengths varied by less than 2% of the original CAI models. This is in contrast to the role of matrix cracking in delamination initiation and individual delamination formation in laminates under transverse loading, where the matrix cracks play an important role [30,35]. It is true that delamination growth starts from the periphery of the pre-existing delaminations, where matrix cracks are already present, but its growth is predominately governed by the stability of the plies in the delaminated regions rather than the presence of the matrix cracks. This suggests that cohesive elements for modelling matrix cracking may not be a critical element in CAI simulations, however they are necessary for accurate predictions of the impact and indentation induced damage that is inserted.

6.2.4 Ply-block Effects

Experimental results showed that the Ss laminates tend to have slightly shallower dent and bulge compared to that of the Ps case for given delamination areas (see Figure 3b). The predictions of the CAI strength of the Ss laminates for given delamination areas were slightly higher than that of the Ps laminates. In the first CAI damage growth events, delaminations grow at the interfaces near the bottom surface. The experimental results for the indented and impacted Ss laminates show that they have smaller delaminations at the bottom interfaces compared to the Ps case for a given delamination area, which is also captured by the high-fidelity indentation models [35]. This leads to less prominent back face bulging in the CAI failure of the Ss laminates (see Figure 6). Consequently, delamination growth at the bottom interfaces requires a

higher compressive load for the Ss laminate than the Ps case, which was also captured by the CAI models. In addition to the differences in delamination morphology between Ss and Ps, for accurate predictions, a smaller magnitude of surface dent and bulge was modelled in the Ss CAI laminate models compared to the Ps models. It is believed the slightly higher compressive strength in the Ss case may also be partially attributed to the less prominent surface imperfections. This delays the delamination growth in the undamaged cone region and, in turn, the associated local buckling.

7 Conclusions

In this study the Compression After Impact (CAI) performance of two laminate configurations with different sizes of damage, that were induced by either low-velocity impact or quasi-static indentation, were examined. Full-field 3D-DIC measurements covering both surfaces at different frame rates during the CAI tests were performed. The DIC results were extremely useful not only for the best quality possible experimentation but also for quantitative model validation of the damage tolerance predictions.

The Ss laminate has higher impact resistance compared to the blocked-ply Ps case, leading to smaller delaminations for the same impact energy, and it was also found to have a higher damage tolerance for small delamination areas. This difference decreased as damage size increased. The CAI strength correlates better with impact energy and delamination area than with the dent depth.

Numerical analysis using high-fidelity finite element models previously used for static indentation [30] and low velocity impact [35] were modified and used for CAI virtual testing. Delaminations from the initial indentation/impact event were carried over and surface imperfections from the indentation/impact (as observed during the experiments) were introduced. The CAI models are able to capture the delamination growth and local buckling behaviour during the CAI failure. The damage sequence and damage mechanisms were analysed. Based on the test results, DIC analysis, similar experimental observations available in the literature and the well validated high-fidelity numerical models, the CAI failure mechanisms and damage evolution of laminates with impact or indentation damage can be summarised as the following (in the order of failure sequence):

- Steady loading stage with a constant buckling stiffness.
- The progression of the initial dent and bulge; the occurrence of local buckling of the delaminated region, which corresponds to a knee point in the central-point deflection curves and the divergence between front and back faces (‘gap between two curves’).
- Delamination propagation and delaminated plies buckling near back face of the laminate.

- Delaminations grow into the undamaged cone, leading to complete delaminated regions and a surface bulge near the dent region forms, due to asymmetric underlying delamination and misalignment between the loading plane and surface geometry.
- The fully delaminated and buckled region propagates rapidly and unstably in the lateral direction to the plate edges, accompanied by a surface bulge.
- Excessive ply strain after catastrophic delamination propagation causes most of the ply fractures.

8 References

[1] Davies GAO, Zhang X. Impact damage prediction in carbon composite structures. International Journal of Impact Engineering 1995;16:149–70.

[2] Bergan A, Bakuckas JG, Lovejoy A, Jegley D, Linton K, Korkosz G, et al. Full-Scale Test and Analysis Results of a PRSEUS Fuselage Panel to Assess Damage Containment Features. Aircraft Airworthiness and Sustainment Conference, 2012, p. 1–17.

[3] Abrate S. Impact on Laminated Composites: Recent Advances. Applied Mechanics Reviews 1994;47:517.

[4] Pavier MJ, Clarke MP. Experimental techniques for the investigation of the effects of impact damage on carbon-fibre composites. Composites Science and Technology 1995;55:157–69.

[5] Cantwell W, Morton J. Comparison of the low and high velocity impact response of CFRP. Composites 1989;20:545–51.

[6] Sanchez-Saez S, Barbero E, Zaera R, Navarro C. Compression after impact of thin composite laminates. Composites Science and Technology 2005;65:1911–9.

[7] ASTM D7136 / D7136M. Standard Test Method for Measuring the Damage Resistance of a Fiber-Reinforced Polymer Matrix Composite to a Drop-Weight Impact Event 2003.

[8] ASTM D7137/D7137M-12 Standard Test Method for Compressive Residual Strength Properties of Damaged Polymer Matrix Composite Plates. West Conshohocken, PA: 2012.

[9] Lawrence B, Emerson R. A Comparison of Low-Velocity Impact and Quasi-Static Indentation. Army Research Laboratory 2012;ARL-TR-627.

[10] Aoki Y, Suemasu H, Ishikawa T. Damage propagation in CFRP laminates subjected to low velocity impact and static indentation. Advanced Composite Materials 2007;16:45–61.

[11] Kaczmarek H, Maison S. Comparative ultrasonic analysis of damage in CFRP under static indentation and low-velocity impact. Composites Science and Technology 1994;51:11–26.

[12] Cartié DDR, Irving PE. Effect of resin and fibre properties on impact and compression after impact performance of CFRP. Composites Part A: Applied Science and Manufacturing 2002;33:483–93.

[13] Guild FJ, Hogg PJ, Prichard JC. A model for the reduction in compression strength of continuous fibre composites after impact damage. Composites 1993;24:333–9.

[14] Ishikawa T, Sugimoto S, Matsushima M, Hayashi Y. Some experimental findings in compression-after-impact (CAI) tests of CF/PEEK (APC-2) and conventional CF/epoxy flat plates. Composites Science and Technology 1995;55:349–63.

[15] Reis L, de Freitas M. Damage growth analysis of low velocity impacted composite panels. Composite Structures 1997;38:509–15.

[16] Aymerich F, Priolo P. Characterization of fracture modes in stitched and unstitched cross-ply laminates subjected to low-velocity impact and compression after impact loading. International Journal of Impact Engineering 2008;35:591–608.

[17] Ghelli D, Minak G. Low velocity impact and compression after impact tests on thin carbon/epoxy laminates. Composites Part B: Engineering 2011;42:2067–79.

[18] Remacha M, Sánchez-Sáez S, López-Romano B, Barbero E. A new device for determining the compression after impact strength in thin laminates. Composite Structures 2015;127:99–107.

[19] Amaro a. M, Reis PNB, de Moura MFSF, Neto M a. Buckling analysis of laminated composite plates submitted to compression after impact. Fibers and Polymers 2014;15:560–5.

[20] Abrate S. Impact on composite structures. Cambridge University Press; 2005.

[21] Suemasu H. Effects of Multiple Delaminations on Compressive Buckling Behaviors of Composite Panels. Journal of Composite Materials 1993;27:1172–92.

[22] Bull DJ, Spearing SM, Sinclair I. Observations of damage development from compression-after-impact experiments using ex situ micro-focus computed tomography. Composites Science and Technology 2014;97:106–14.

[23] Nilsson K, Asp L, Alpman J, Nystedt L. Delamination buckling and growth for delaminations at different depths in a slender composite panel. International Journal of Solids and Structures 2001;38:3039–71.

[24] Asp LE, Nilsson S, Singh S. An experimental investigation of the influence of delamination growth on the residual strength of impacted laminates. Composites - Part A: Applied Science and Manufacturing 2001;32:1229–35.

[25] Short G., Guild F., Pavier M. The effect of delamination geometry on the compressive failure of composite laminates. Composites Science and Technology 2001;61:2075–86.

[26] Hwang S -f., Mao C -p. Failure of Delaminated Carbon/Epoxy Composite Plates under Compression. Journal of Composite Materials 2001;35:1634–53.

[27] Pérez M a., Gil L, Sánchez M, Oller S. Comparative experimental analysis of the effect caused by artificial and real induced damage in composite laminates. Composite Structures 2014;112:169–78.

[28] Zhou G. Investigation for the Reduction of In-plane Compressive Strength in Preconditioned Thin Composite Panels. Journal of Composite Materials 2005;39:391–422.

[29] Rivallant S, Bouvet C, Abi Abdallah E, Broll B, Barrau J-J. Experimental analysis of CFRP laminates subjected to compression after impact: The role of impact-induced cracks in failure. Composite Structures 2014;111:147–57.

[30] Sun XC, Wisnom MR, Hallett SR. Interaction of inter- and intralaminar damage in scaled quasi-static indentation tests: Part 2 – Numerical simulation. Composite Structures 2016;136:712–26.

[31] Abisset E, Daghia F, Sun XC, Wisnom MR, Hallett SR. Interaction of inter- and intralaminar damage in scaled quasi-static indentation tests: Part 1 – Experiments. Composite Structures 2016;136:712–26.

[32] Hallett SR, Wisnom MR. Numerical Investigation of Progressive Damage and the Effect of Layup in Notched Tensile Tests. Journal of Composite Materials 2005;40:1229–45.

[33] Wisnom MR, Khan B, Hallett SR. Size effects in unnotched tensile strength of unidirectional and quasi-isotropic carbon/epoxy composites. Composite Structures 2008;84:21–8.

[34] Hallett SR, Jiang W-G, Khan B, Wisnom MR. Modelling the interaction between matrix cracks and delamination damage in scaled quasi-isotropic specimens. Composites Science and Technology 2008;68:80–9.

[35] Sun XC, Hallett SR. Barely Visible Impact Damage in Scaled Composite Laminates: Experiments and Numerical Simulations. International Journal of Impact Engineering 2017;109.

[36] Mukhopadhyay S, Jones MI, Hallett SR. Compressive failure of laminates containing an embedded wrinkle; experimental and numerical study. Composites Part A: Applied Science and Manufacturing 2015;73:132–42.

[37] Lee J, Soutis C. Measuring the notched compressive strength of composite laminates: Specimen size effects. Composites Science and Technology 2008;68:2359–66.

[38] Bouvet C, Rivallant S, Barrau JJ. Low velocity impact modeling in composite laminates capturing permanent indentation. Composites Science and Technology 2012;72:1977–88.

[39] Abdallah EA, Bouvet C, Rivallant S, Broll B, Barrau J-J. Experimental analysis of damage creation and permanent indentation on highly oriented plates. Composites Science and Technology 2009;69:1238–45.

[40] He W, Guan Z, Li X, Liu D. Prediction of permanent indentation due to impact on laminated composites based on an elasto-plastic model incorporating fiber failure. Composite Structures 2013;96:232–42.

[41] Shi Y, Swait T, Soutis C. Modelling damage evolution in composite laminates subjected to low velocity impact. Composite Structures 2012;94:2902–13.

[42] Hwang S-F, Liu G-H. Buckling behavior of composite laminates with multiple delaminations under uniaxial compression. Composite Structures 2001;53:235–43.

[43] de Freitas M, Reis L. Failure mechanisms on composite specimens subjected to compression after impact. Composite Structures 1998;42:365–73.

[44] Hexcel Composites. HexPly® 8552 Epoxy matrix (180°C/356°F curing matrix) Product Data. 2000.

[45] O'Brien T, Johnston W, Toland G. Mode II interlaminar fracture toughness and fatigue characterization of a graphite epoxy composite material. NASA Langley Research Center; Hampton, VA, United States: 2010.

[46] Hallett SR, Green BG, Jiang WG, Wisnom MR. An experimental and numerical investigation into the damage mechanisms in notched composites. Composites Part A: Applied Science and Manufacturing 2009;40:613–24.

9 Figures

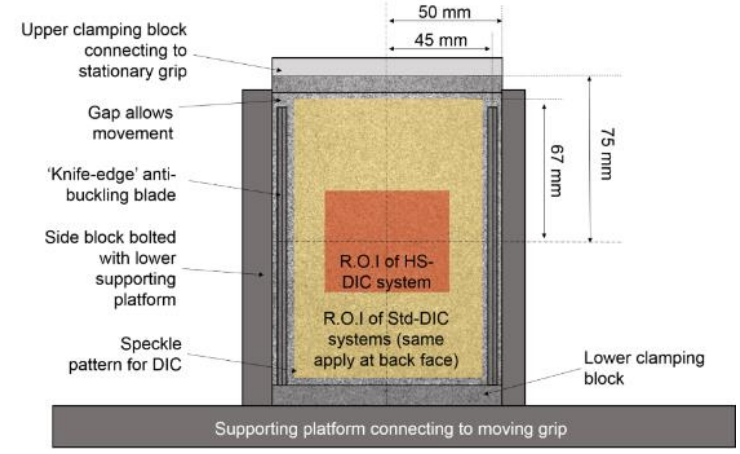

(a)

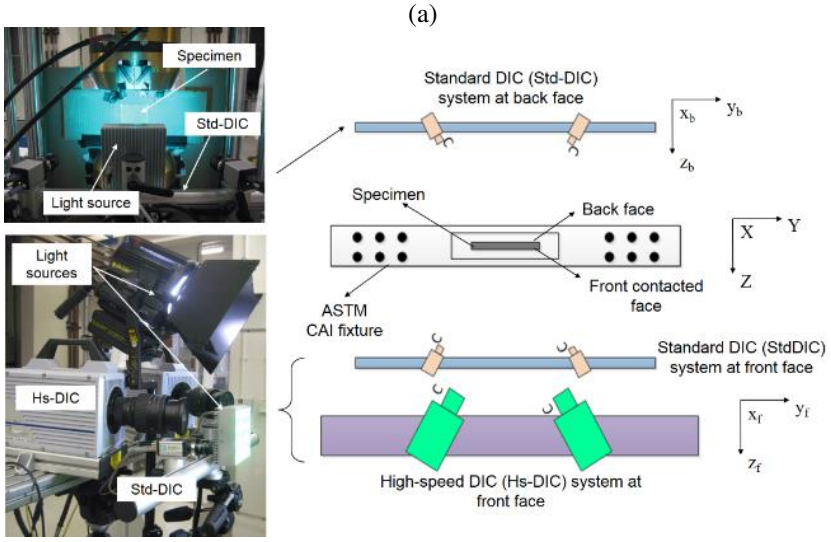

(b)

Figure 1 (a) Illustration of CAI fixture front face showing different Region of Interest (ROI) for Std-DIC systems and HS-DIC system. (b) Experimental setup (left) and schematic (right) of the arrangement of three 3D-DIC systems for CAI testing. (The front-face setup is shown in the lower left and back-face setup in the upper left).

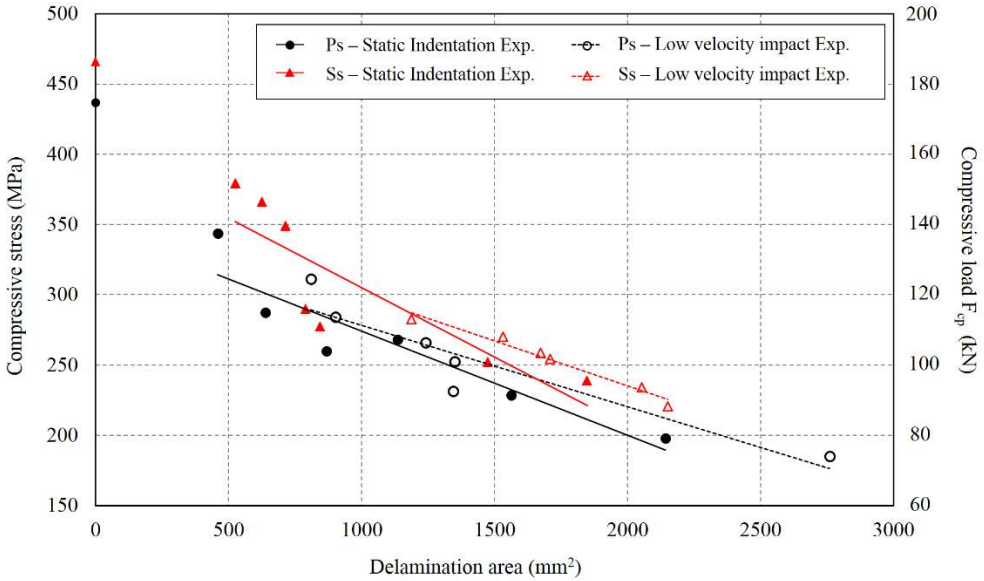

Figure 2: Delamination area vs. residual compressive strength for the two types of laminates with low-velocity impact and static indentation damage.

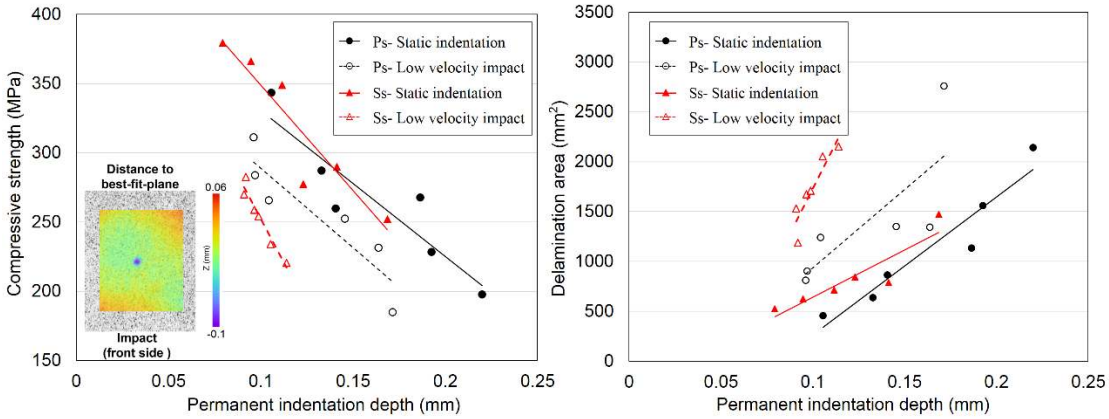

(a) (b)

Figure 3 (a) Permanent indentation depth vs. residual compressive stress, also showing the DIC results for dent depth measurement. (b) Permanent indentation depth vs. delamination area

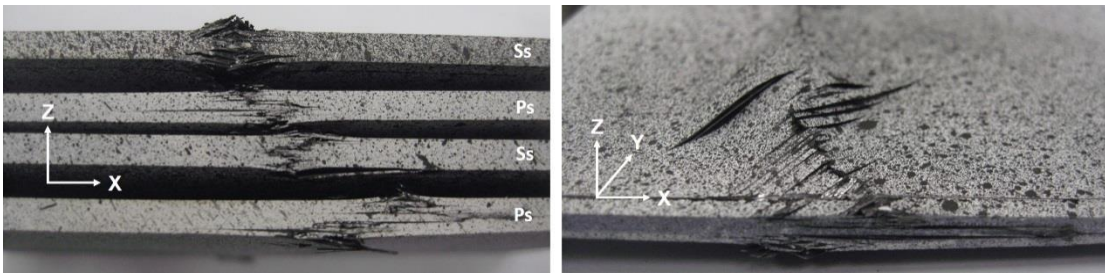

(a) (b)

Figure 4: (a) Side view of four specimens failed by CAI tests from top to bottom; Ss, Ps, Ss and Ps laminates. (b) Fibre fracture at front surface after CAI failure in a post-impact Ps laminate. Note that there is no obvious differences of final ruptured states laminate with single and double plies damaged by low-velocity impact or static indentation.

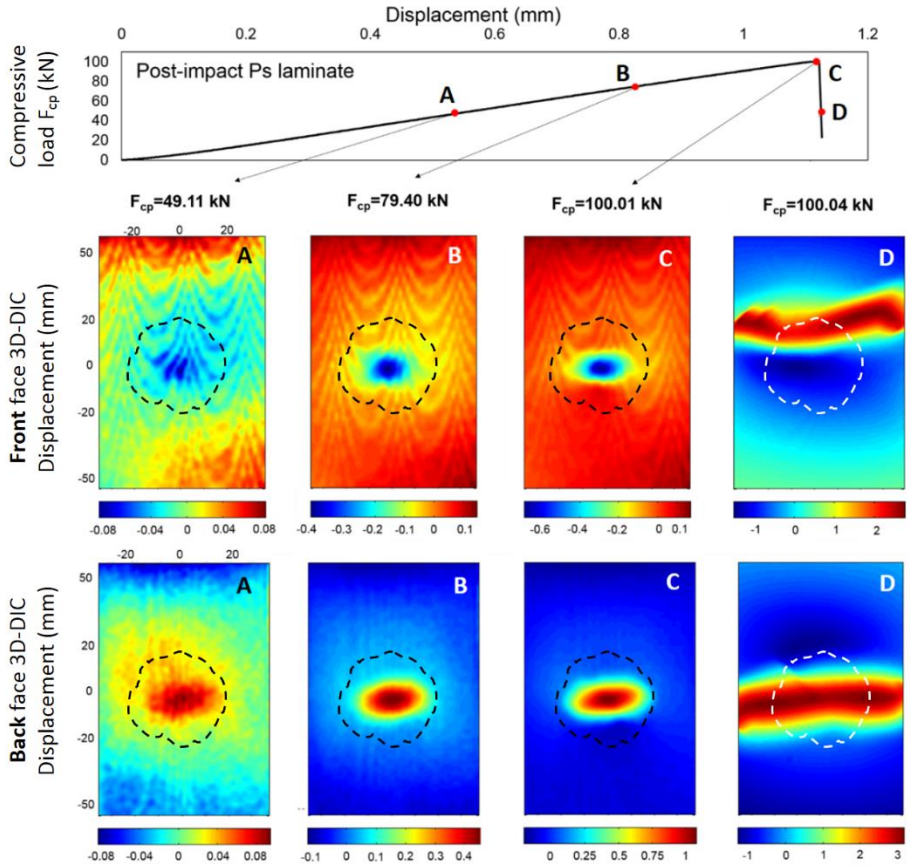

Figure 5: Out-of-plane front and back face deflection contour for Ps laminate at four different loading stages indicated on the load-displacement curve from the CAI test; the initial damage was a result of 12 J impact, and the post-impact delamination profile is illustrated by dashed line.

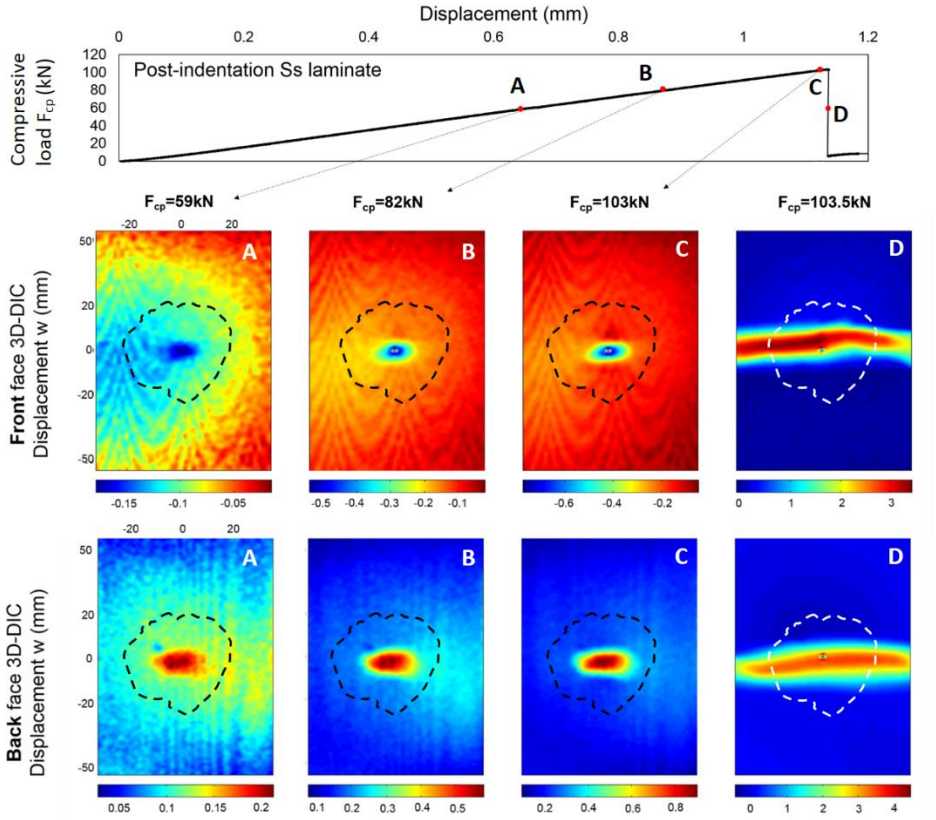

Figure 6: Post-indentation Ss laminate DIC result of front and back face out-of-plane deflection contour at four different loading stages indicated the load-displacement plot at the top during CAI test; The Ss laminate was loaded up to 6.5 kN during static indentation, and the post-indentation delamination profile is illustrated by dashed line.

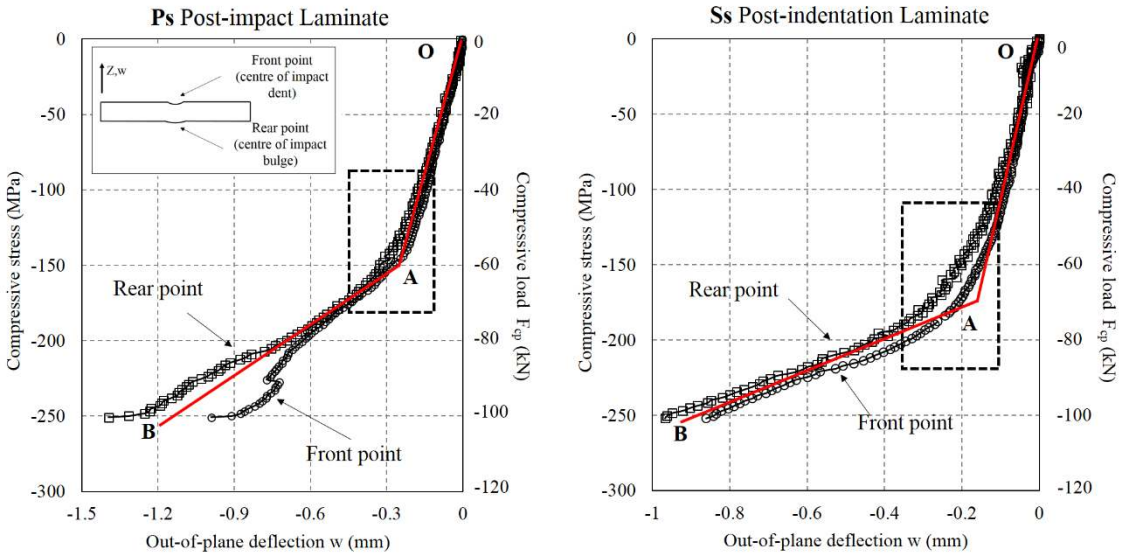

Figure 7 Plate central point out-of-plane deflection of Ps (Left i.e. the case of Figure 5) and Ss (Right i.e. the case of Figure 6) vs. compressive stress during CAI test, measured by DIC system. The front central point delfecting to the opposite direction at the final failure stage is neglected. Note that 'A' is referring to 'knee point', a intersection of the two linear trand lines.

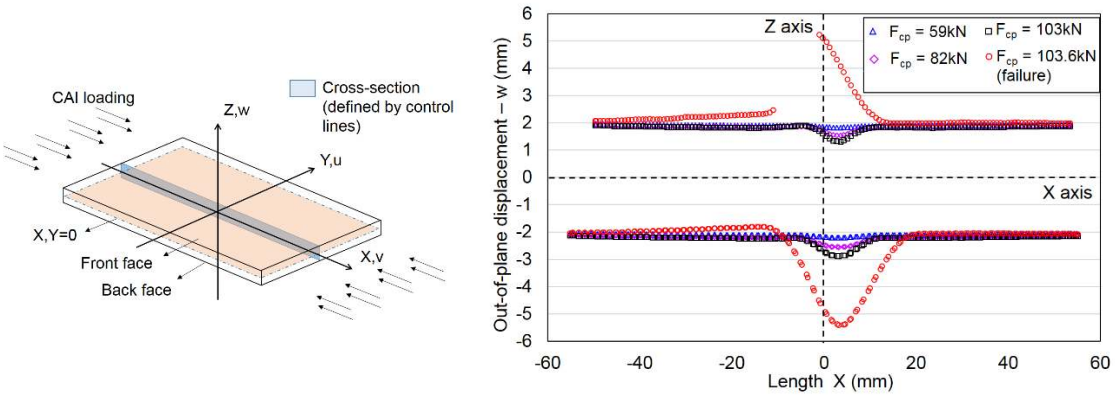

(a) (b)

Figure 8: (a) Laminate in global coordinates showing loading and control line location (b) Progressive cross-section change of post-identation Ps laminate under a increasing compressive load.

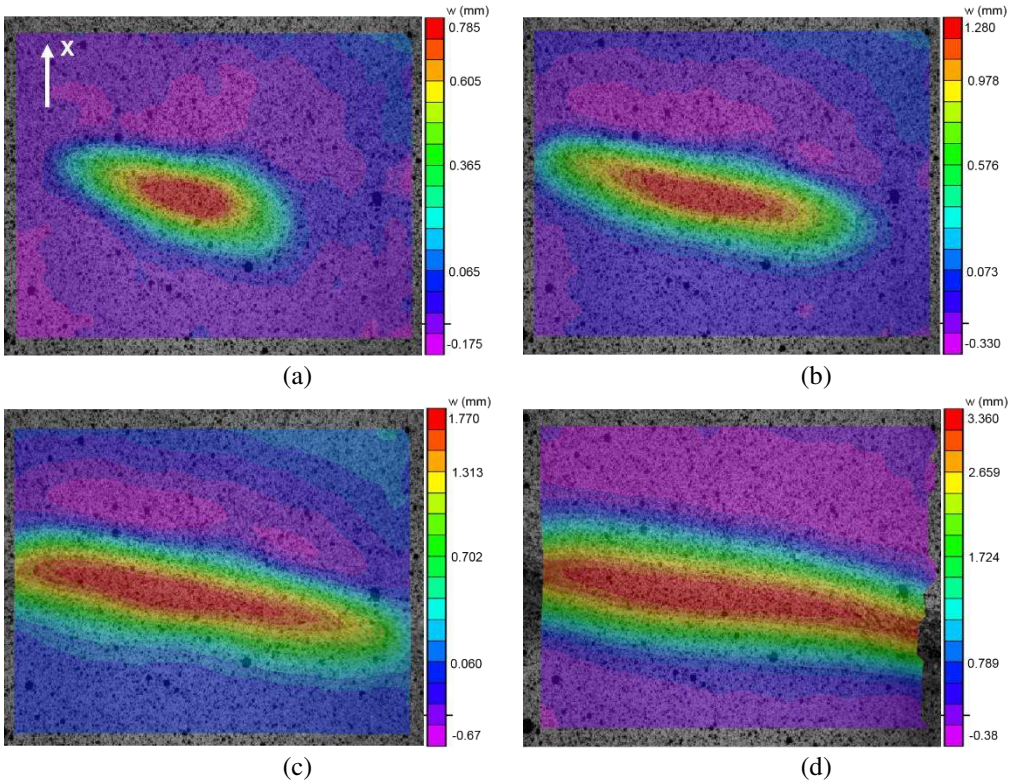

Figure 9: Back face out-of-plane displacement contour plots (relative to the reference frame) for impact damaged Ss laminates measured by Hs-DIC system at four consecutive frames from (a)-(d). The time interval between frames is 0.06 ms

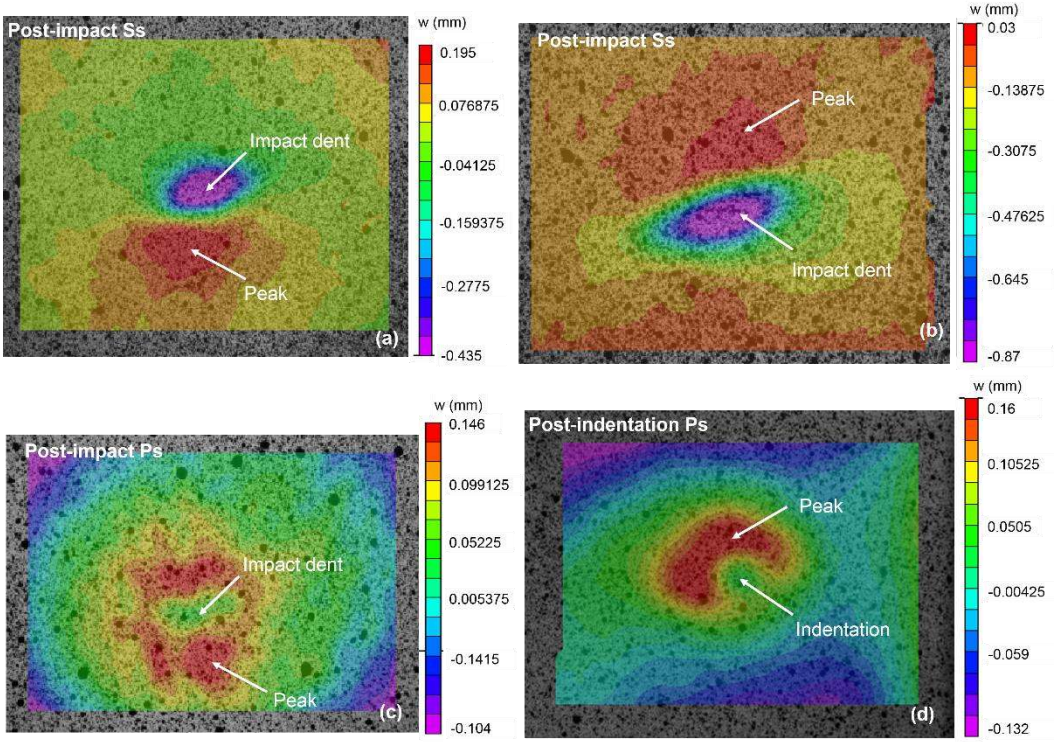

Figure 10: Front face out-of-plane displacement contour plots (relative to the reference frame and captured at the first frame after the Hs-DIC is triggered) for impact and static indentation damaged Ps and Ss laminates.

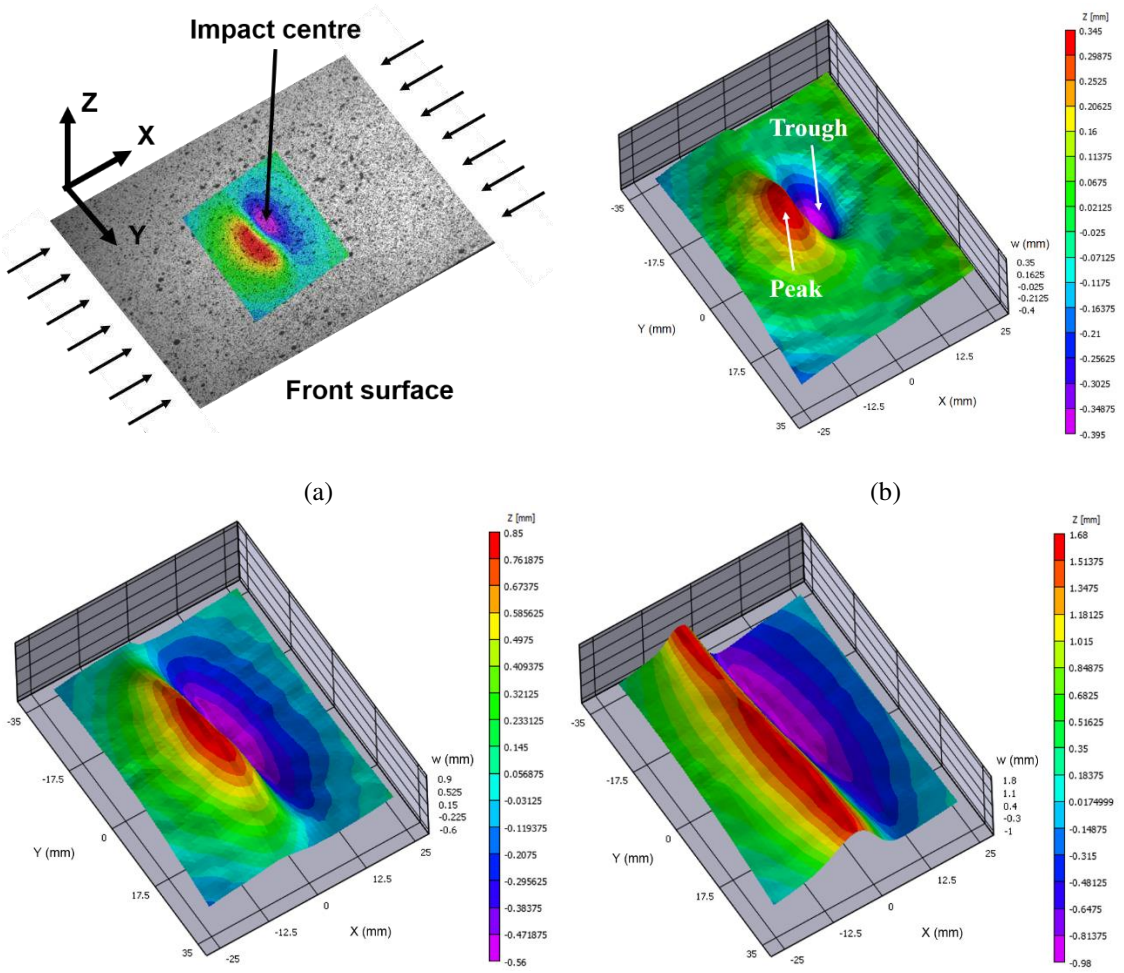

Figure 11 (a) Observation window of Hs-DIC system relative to the overall observable plate area. Front face out-of-plane displacement contour plots (relative to the reference frame) for post-impact Ps laminates measured by Hs-DIC system at three consecutive frames from (b)-(d) with time interval about 0.06 ms.

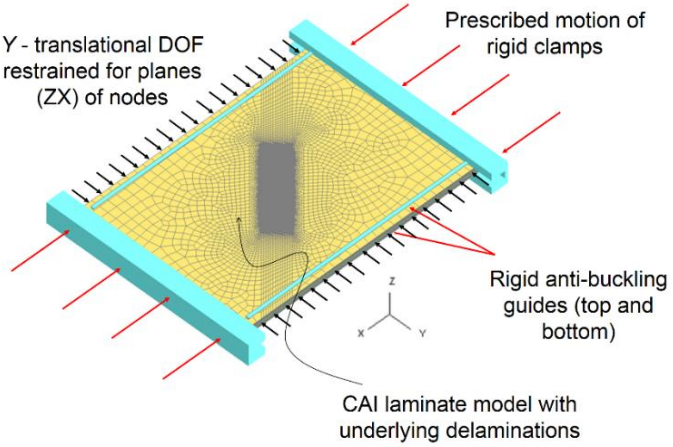

Figure 12 CAI modelling configuration.

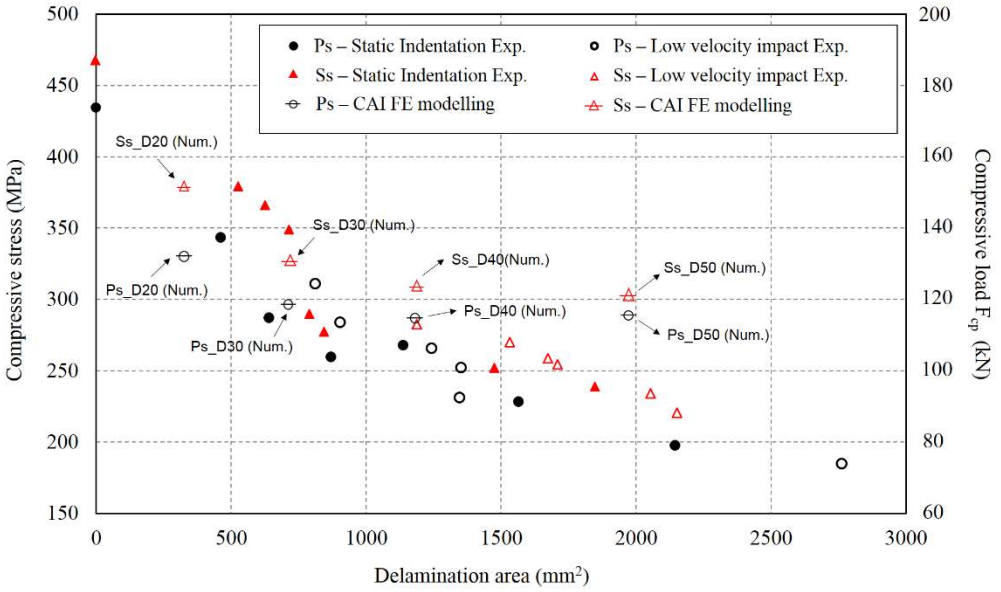

Figure 13 Delamination area vs. residual compressive strength for Ps and Ss laminates, both low-velocity impact and static indentation tests, with corresponding numerical modelling resutls.

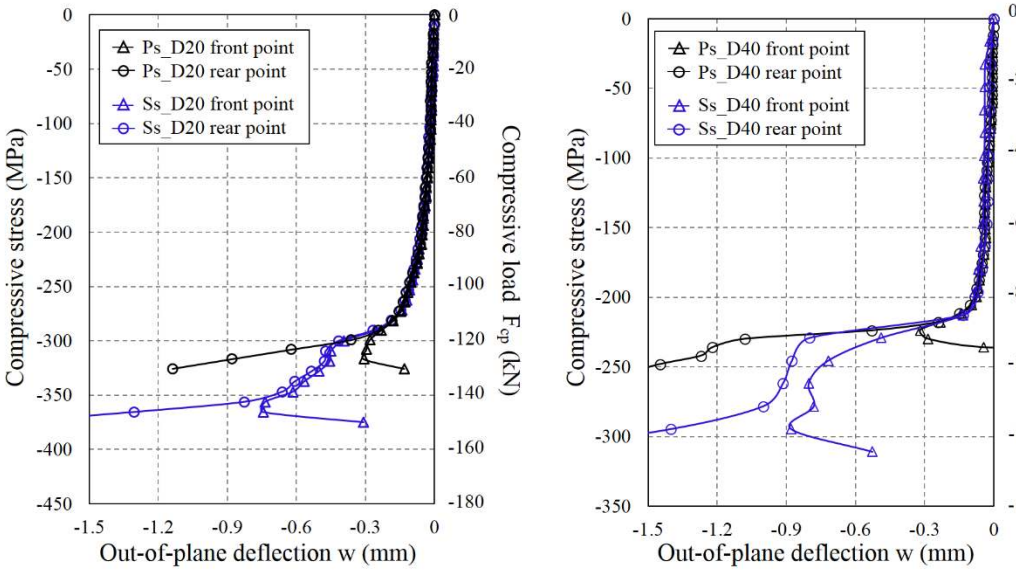

(a) (b)

Figure 14 Plate model central point out-of-plane deflection of (a): Ps_D20/Ss_D20 and (b) Ps_D40/Ss_D40 cases vs. compressive stress (load) obtained from CAI modelling.

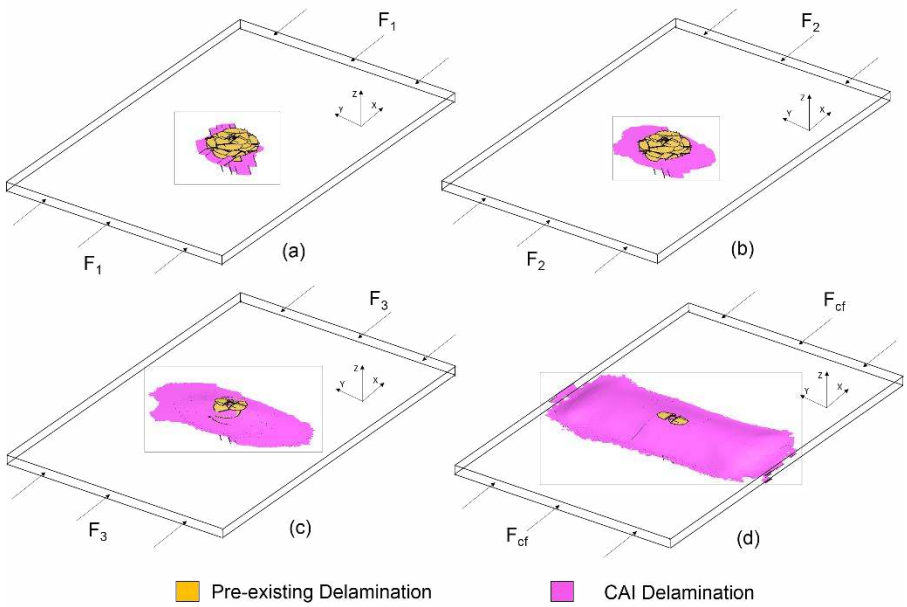

Figure 15: Delamination propagation of a Ps_D20 case during CAI simulation. The pre-existing delamination introduced by the virtual static indentation test and delamination created during CAI are highlight in diffferent colours. (a-d) delamination propagation at compression F_1, F_2, F_3 and F_{cf}.

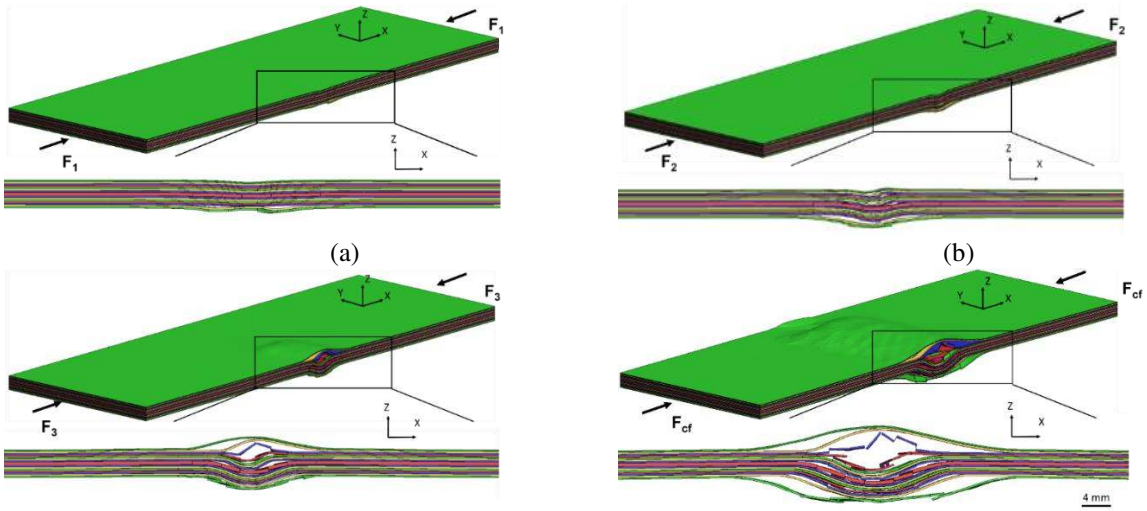

Figure 16: Longitudinal cut-section views through the centre of the initial damage during CAI simulation of the Ps_D20 case at the four previously defined load levels a) F1, b) F2, c) F3 and d) at the compressive failure load F_{cf}.

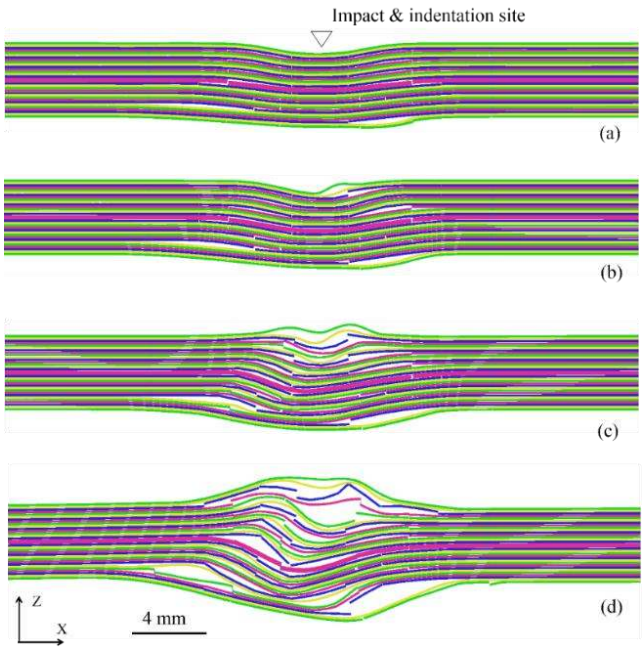

Figure 17: Progressive longitudinal cross section views through the centre of the initial damage during CAI simulation of the Ss_D20 case at four load levels from (a) to (d). (d) is showing the cross-section of at the final compressive failure stage.

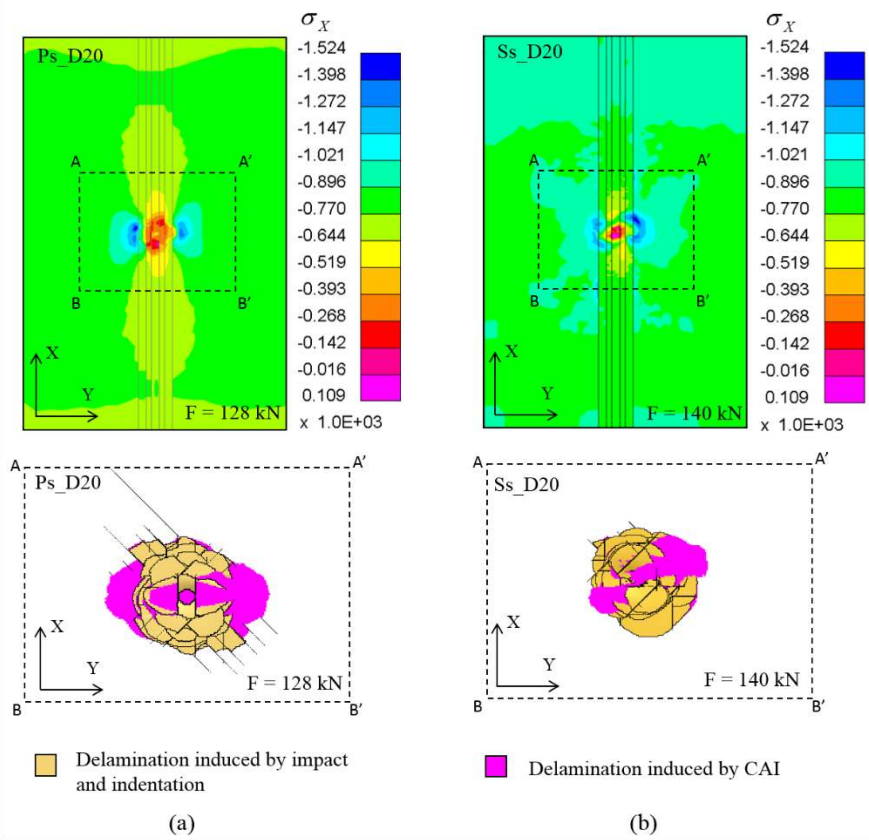

Figure 18: Fibre direction stress contour plots for load bearing 0° ply at major delamination propagation (a) Ps_D20 CAI model; (b) Ss_D20 CAI model; shown with corresponding delamination state

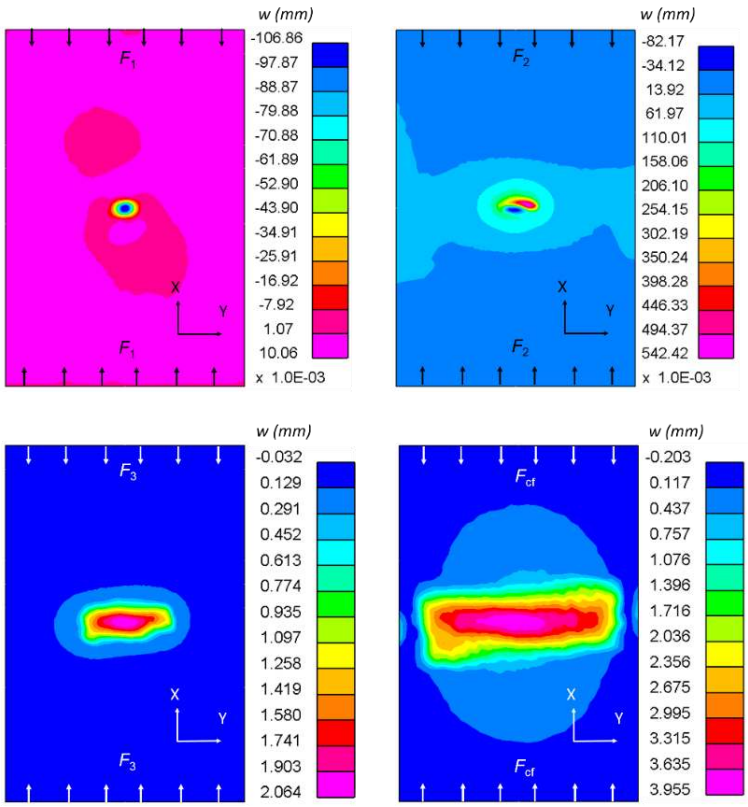

Figure 19: Ps laminate CAI modelling results of front face out-of-plane deflection contour at four different loading stages indicated in Figure 15 and Figure 16.

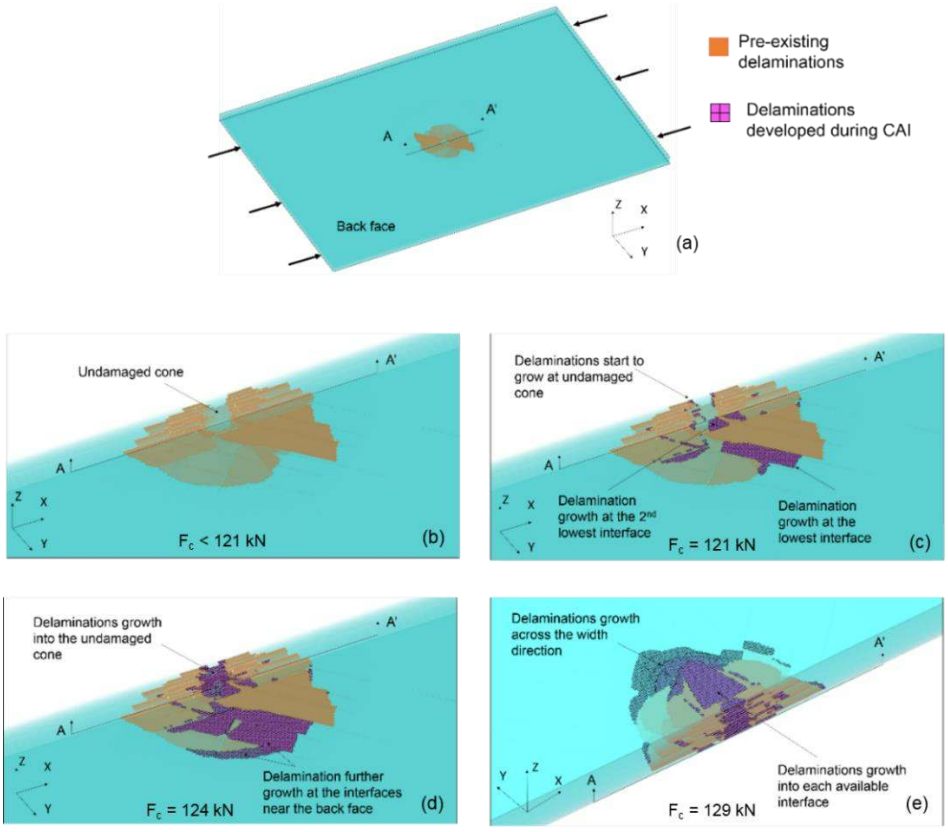

Figure 20 The simulation results of detailed delaminaiton evolution during CAI failure of Ps_D20 model. The laminate is based on undeforemd state before CAI loading starts. (a) plate oriation and figure legend, (b) pre-exisitng delamination and delamination-free zone resulted from impact/indentation simulation, (c-e) delamination evolution as compression increases.

10 Tables

Table 1 Material properties of IM7/8552 [45,46] adopted for modelling. See [35] for details.

Ply properties	Interface Properties
$E_{11} = 161\,GPa \quad E_{22} = E_{33} = 11.4\,GPa$	$E_I = E_{II} = 100\,GPa$
$\upsilon_{12} = 0.3 \quad \upsilon_{23} = 0.436$	$\sigma_I^* = 60\,MPa \quad \sigma_{II}^* = 90\,MPa$
$G_{12} = G_{13} = 5.17\,GPa \quad G_{23} = 3.98\,GPa$	$G_{IC} = 0.2\,N/mm \quad G_{IIC} = 0.8\,N/mm$
$\alpha_{11} \approx 0 \quad \alpha_{22} = \alpha_{33} = 3 \cdot 10^{-5}$	$\alpha = 1 \quad \phi = 0.58$
$\rho = 1.6\,g/cm^3$	$\rho = 1.0\,g/cm^3$